energies

MDPI

Article

An Inherent Decoupled Triple-Active Bridge Converter for All-Electric Aircraft DC Power Systems

Giuseppe Bossi [1], Nicola Campagna [2], Mauro Boi [1], Rosario Miceli [2] and Alfonso Damiano [1,*]

[1] Department of Electrical and Electronic Engineering, University of Cagliari, Via Marengo 2, 09124 Cagliari, Italy; giuseppe.bossi@unica.it (G.B.); mauro.boi@unica.it (M.B.)
[2] Department of Engineering, University of Palermo, Viale delle Scienze, Ed. 8, 90133 Palermo, Italy; nicola.campagna@unipa.it (N.C.); rosario.miceli@unipa.it (R.M.)
* Correspondence: damiano@unica.it

Abstract: This paper focuses on a power conditioning system for an all-electric aircraft (AEA) powered by a single battery pack. The research project aims to identify a multi-port DC/DC converter topology that adequately supplies the two DC buses connected to the propulsion system and auxiliary equipment, respectively. To achieve this, a triple-active bridge (TAB) in its inherently decoupled configuration has been investigated, prototyped, and experimentally verified. The TAB voltage control system was designed, simulated, and experimentally validated. Specifically, start-up, steady-state and step-load performances were evaluated by the simulation study and then experimentally validated on a scaled prototype. The results assess the feasibility of using an inherently decoupled TAB as a power conditioning system for interconnecting the AEA battery pack with the electric propulsion and auxiliary systems. In particular, the developed TAB configuration secures the decoupled power transfer between the two output ports providing at the same time good dynamic performance in terms of voltage control during step-load variation.

Keywords: DC/DC converters; triple-active bridge; energy storage systems; all-electric aircraft

Citation: Bossi, G.; Campagna, N.; Boi, M.; Miceli, R.; Damiano, A. An Inherent Decoupled Triple-Active Bridge Converter for All-Electric Aircraft DC Power Systems. *Energies* **2024**, *17*, 6368. https://doi.org/10.3390/en17246368

Academic Editor: Miguel Castilla

Received: 16 October 2024
Revised: 12 December 2024
Accepted: 16 December 2024
Published: 18 December 2024

1. Introduction

The All-electric aircraft (AEA) is considered one of the most promising solutions to mitigate the impact of greenhouse gas emissions in the aviation industry. The AEA eliminates the production of harmful gases during flight by not using fossil fuels to power propulsion and auxiliary systems [1]. The main feature of the AEA is the exclusive employment of electricity for supplying all the equipment involved in aircraft flight missions [2]. Regarding the propulsion system, the AEA has a much higher efficiency than fossil fuel engines. This result is mainly ascribed to the usage of electric drives as movers for propellers, implementing Distributed Electric Propulsion (DEP) configurations. This solution is remarkably quiet and light. In addition, the DEP system offers a higher level of redundancy than traditional systems and performs well even in off-flight situations [3].

However, the main AEA issue is the availability of equipment that can provide energy and power in all possible operating conditions of commercial flight paths while maintaining aeronautical safety standards. The solutions proposed for providing AEA supply are based on hydrogen conversion or energy storage systems (ESSs). The first one concerns the use of liquid hydrogen converted into electricity by using fuel cells or hydrogen-based combustion engines. The second one resorts to electrochemical batteries or hybrid configurations integrated with supercapacitors and/or fuel cells [4,5].

With regard to the battery-based configuration, the feasibility studies carried out on the original design of the Airbus A320 have defined its AEA-optimised version. The AEA version of the A320 has a range of 925 km, assuming a battery gravimetric energy density (GED) of 800 Wh/kg. Nevertheless, the maximum take-off weight assumes a value of 109.5 tons, 65% more than actual ones. Moreover, the power and propulsion systems,

including ESS, are four times heavier than that installed in the conventional Airbus A320, including fuel [6]. Nevertheless, the actual electrochemical batteries achieve a maximum GED of 450 Wh/kg, making the complete electric conversion of the avionic sector unfeasible. On the other hand, the battery GED target of 800 Wh/kg could be attained shortly by means of solid-state and lithium-sulphur batteries [7,8].

For these reasons, the research and prototyping activities on this topic are primarily focused on ultra-light aircraft (ULA) and light sport aircraft (LSA), because they can fix design objectives in terms of the flight path, maximum take-off weight, peak power and energy demand achievable by the available electrochemical ESS [9].

In this context, the authors have been involved in a project to develop an innovative electric propulsion and auxiliary power system for a light horizontal take-off and landing (HTOL) aircraft with a flight autonomy of one hundred km [5]. In particular, the project aims to design a high-performance power conditioning system for supplying AEA with a single battery pack.

A solution already proposed in the technical literature for AEA is the implementation of multiple DC/DC power converters as dual active bridges (DAB). It achieves high power conversion efficiency and allows individual power control. However, there is an increase in the number of devices and a decrease in the power density [10]. To this end, several architectures have been proposed with a view to the reduction of the number of power conversion stages [11]. Most studies available in the literature tend to focus on optimising the propulsion system [12–14] to improve the overall system efficiency. However, this approach often neglects the power supply for auxiliary services. This separation in management implies that auxiliary services require a dedicated energy source, typically provided by a secondary storage system (dedicated batteries) and an additional converter to adjust the required voltage or current level. Such a configuration can introduce further challenges, including the total system weight increasing, the complexity of the electrical architecture and the reduction of the overall system efficiency. In this context, the multi-active bridge (MAB) converter appears to be a viable solution for increasing the power density of electronic conversion systems and reducing the overall number of components.

In addition, MAB converters are particularly suitable when the power system has different DC voltage standards, such as in the avionics sector. In fact, aircraft voltage standards specify different AC and DC values depending on the field of application. Nevertheless, the trend is to replace traditional AC distribution with DC one characterised by only two DC buses: a high DC-voltage bus at 270 V_{dc} and a lower one at 28 V_{dc} [11,15]. Moreover, the MAB converters permit the power management of multi-sources configurations and the compensation of voltage variation occurring on the battery during discharging and peak power demand [16]. However, the usage of MAB introduces interdependencies among its ports due to their magnetic coupling, increasing consequently the complexity of its power management. These effects require the introduction of decoupling strategies. The solutions proposed in the technical literature follow two approaches. The first one resorts to the use of decoupling control algorithms synthesised from TAB modelling [16]. The second approach is hardware-based and allows for inherent decoupling by adequately designing the MAB [17].

This work proposes a triple-active bridge (TAB) design methodology aimed at mitigating the coupling effects and achieving "*quasi-decoupling*" of power flows between the input and the two output ports. Specifically, a TAB converter topology was investigated to supply the AEA propulsion and auxiliary power systems.

The proposed modelling allows for the correct design of the external leakage inductances, considering the effects of medium frequency transformer leakage inductances.

The designed configuration was simulated and experimentally validated to demonstrate the feasibility of independently managing the output power of TAB under specific constraints. An extended analysis of the start-up and step-load behaviour of the TAB is carried out to emulate the demand occurring in the propulsion and auxiliary systems of

an AEA. Finally, the simulation and experimental results are compared to validate the proposed modelling and confirm the validity of the proposed configuration.

In particular, Section 2 describes the model of TAB; Section 3 reports the structure of the AEA power supply system with the proposed TAB configuration; in Section 4, the experimental set-up is described; the comparison between the simulation and experimental results is reported in Section 5, and finally, Section 6 reports the concluding remark.

2. Triple-Active Bridge

The TAB is a bidirectional buck–boost DC/DC converter. Its topology uses three active bridges connected by a three-winding medium-frequency transformer (MFT). The schematic structure of the TAB is shown in Figure 1. The operating principle is based on implementing a DC/AC and AC/DC conversion process between each port, which allows power and voltage conditioning with high efficiency [18]. Specifically, the modulation of active bridges generates three square wave voltages with a 50% duty cycle at a fixed switching frequency f_s. The voltage and power control are achieved by managing the phase shift δ_{ij} between the voltage j active bridge concerning i one [19]. This specific TAB modulation technique is known as single phase shift (SPS). Its advantages are simplicity and the achievement of soft switching conditions in well-defined operating conditions; its disadvantages are the presence of high peak currents on the MFT and flow-back currents on the output DC side. In addition, the soft switching and the zero re-circulation power conditions impose limitations on voltage and power set-points. Advanced modulation techniques, such as double-phase and triple-phase shifts, overcome these issues and improve TAB performance. However, they add complexity to the control system [20].

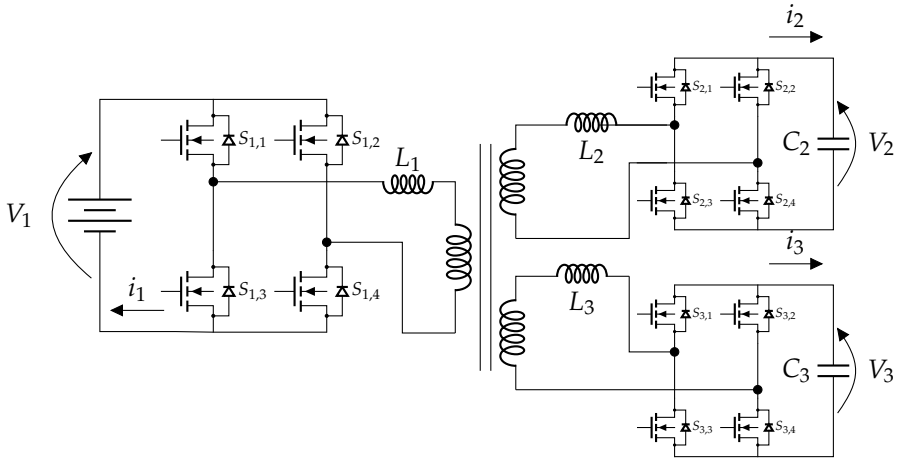

Figure 1. Schematic of a triple-active bridge.

2.1. TAB Model

Considering the TAB structure in Figure 1, its equivalent circuit assumes the topology shown in Figure 2a. In particular, the equivalent circuit consists of a three-winding transformer, represented by the magnetizing inductance L_m and the leakage inductance on each port L_k. This transformer is supplied by three square-wave voltage generators characterized by a defined amplitude and frequency, where the phase displacements serve as the control parameters. The TAB model is developed by considering port no. 1 as a reference. Then, the prime symbol ($'$) is used, in the discussion, to define quantities reported to the reference port. Therefore, the parameters and the electrical quantities (currents and voltages) are referred to port no. 1 using (1), where N_1:N_2 and N_1:N_3 are the respective turns ratios.

$$v'_k = \frac{N_1}{N_k} v_k;\ i'_k = \frac{N_k}{N_1} i_k;\ L'_k = \left(\frac{N_1}{N_k}\right)^2 L_k \quad for\, k = 2,3; \tag{1}$$

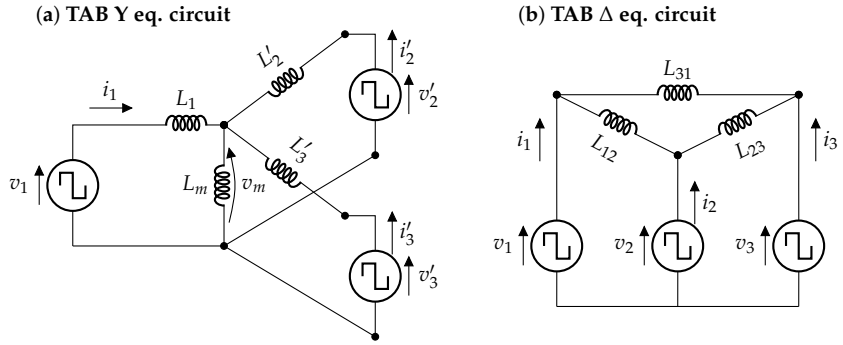

Figure 2. Equivalent circuits of TAB converter.

The magnetising inductance L_m models the magnetic tank coupling the three ports and its value is strictly related to the transformer design. The leakage inductances on each MFT winding can be modified to achieve specific values, L_1, L'_2, and L'_3, by properly adding external inductors.

The magnetizing voltage, v_m, expressed as a function of v_k, is evaluated by applying superposition law. Hence, v_m assumes the form stated by (2), as reported in [21].

$$v_m = \frac{v_1 L'_2 L'_3 + v'_2 L_1 L'_3 + v'_3 L_1 L'_2}{L_1 L'_2 + L_1 L'_3 + L'_2 L'_3} \tag{2}$$

The analysis of the TAB-equivalent circuit reported in Figure 2a shows that the power provided by each generator can be evaluated by referring to DAB modelling, considering the voltage v_m as output. Therefore, the power on each TAB port can be determined by (3)–(5) under the hypothesis of implementing the SPS modulation strategy. V'_2 and V'_3 are the DC bus voltages of the active bridges connected to port no. 2 and no. 3, referred to no. 1, and δ_{jk} is the phase displacement between the square wave voltage applied by k active bridge concerning the j one.

$$P_1 = \frac{V_1 V'_2 L'_3\, \delta_{12}(\pi - |\delta_{12}|) + V_1 V'_3 L'_2\, \delta_{13}(\pi - |\delta_{13}|)}{2\pi^2 f_s (L_1 L'_2 + L_1 L'_3 + L'_2 L'_3)}; \tag{3}$$

$$P_2 = \frac{V_1 V'_2 L'_3\, \delta_{21}(\pi - |\delta_{21}|) + V'_2 V'_3 L_1\, \delta_{23}(\pi - |\delta_{23}|)}{2\pi^2 f_s (L_1 L'_2 + L_1 L'_3 + L'_2 L'_3)}; \tag{4}$$

$$P_3 = \frac{V_1 V'_3 L'_2\, \delta_{31}(\pi - |\delta_{31}|) + V'_2 V'_3 L_1\, \delta_{32}(\pi - |\delta_{32}|)}{2\pi^2 f_s (L_1 L'_2 + L_1 L'_3 + L'_2 L'_3)}; \tag{5}$$

The Y-equivalent circuit simplifies the visualization of power expressions at each port, enhancing clarity in their derivation. It can be transformed into a Δ one, as shown in Figure 2b), enabling a direct understanding of the relationship between power transfer and the presence of cross-coupling effects. Indeed, the inductances L_{jk} can be evaluated by (6) through the leakage inductance L_k. The Δ equivalent circuit allows the determination of the power transfer from the port j port to the k one by (7). Hence, the relationship between the power provided by each active bridge on port k, named P_k and the power transfers between each port P_{jk} assume the form reported in (8) as a consequence of (3)–(5).

$$\begin{cases} L_{12} = L_1 + L'_2 + \dfrac{L_1 L'_2}{L'_3} \\ L_{23} = L'_2 + L'_3 + \dfrac{L'_2 L'_3}{L_1} \\ L_{31} = L_1 + L'_3 + \dfrac{L_1 L'_3}{L'_2} \end{cases} \tag{6}$$

$$P_{jk} = \frac{V_j' V_k'}{2\,\pi^2\, f_s\, L_{jk}} \delta_{jk} \left(\pi - \left|\delta_{jk}\right|\right) \tag{7}$$

$$\begin{cases} P_1 = & P_{12} - P_{31}; \\ P_2 = & P_{23} - P_{12}; \\ P_3 = & P_{31} - P_{23}; \end{cases} \tag{8}$$

The relationships existing between the phase displacement of the square wave voltages δ_{jk} reported in (9) and power ones (7) and (8) highlight the presence of cross-coupling effects which requires the implementation of software or hardware solutions aimed to decouple the power management among the TAB ports [17,19]. Moreover, in order to avoid power losses and maximize efficiency, zero power flow circulation inside the TAB has to be guaranteed. This can be achieved by satisfying the power balance condition reported in (10) and (11). These constraints underline the presence of cross-coupling because the power flows between two ports depend on that provided by the third one.

$$\delta_{23} = \delta_{13} - \delta_{12}; \tag{9}$$

$$P_{12} + P_{23} + P_{31} = 0; \tag{10}$$

$$\begin{cases} P_{12} = & -\frac{2}{3} P_2 - \frac{1}{3} P_3; \\ P_{23} = & -\frac{2}{3} P_3 - \frac{1}{3} P_1; \\ P_{31} = & -\frac{1}{3} P_2 - \frac{2}{3} P_3; \end{cases} \tag{11}$$

2.2. Inherent Decoupled TAB Topology

The inherent cross-coupling of power flows between TAB ports is a key issue for this DC/DC converter class, and its settlement involves the hardware and control design. The technical literature proposes software and hardware solutions to overcome this issue. The software solution refers to the TAB model. Specifically, decoupling algorithms are synthesised, resorting to the implementation of the inverse matrix compensator [19]. A high computational effort and a centralised controller architecture characterise this class of decoupling algorithms. However, they achieve good performance in a wide range of areas.

Another control strategy aimed at achieving TAB decoupling is based on dynamically differentiating implemented control loops by setting different bandwidths. In particular, a specific control state variable is chosen as dominant, and its controller is synthesised to have the highest bandwidth for imposing the phase-shift evolution during transients [16]. This approach reduces the computation effort and allows a decentralised controller design.

Recently, a hardware approach, oriented to decouple the power flow in a multi-active bridge converter inherently, has been proposed [17]. The authors have investigated this configuration because it seems suitable for developing an AEA power conditioning system powered by a single battery pack. The solution proposed consists of removing the external inductor in one port of TAB that assumes the role of *"master"* port and designing properly the MFT and the leakage inductors on the other two. This hardware approach allows for the inherent power decoupling between the TAB's ports without additional components. This hardware configuration makes TAB equivalent to two DABs connected to the same power source (master) and controlled independently. However, the control design requires particular attention due to the asymmetrical topology and the non-linear behaviour.

In order to evaluate the features of inherent decoupled TAB topology, a linearised model has been proposed and then analysed. For this purpose, the general formulation of the power provided to the *k*-isium port, as reported in (12), enables the evaluation of the cycle-by-cycle average (CCA) TAB current I_k under the assumption that the voltages on the active bridges remain constant, as follows:

$$P_k = \sum_{j \neq k} P_{kj} = \sum_{j \neq k}^{3} \frac{V_j' V_k'}{2\,\pi^2\, f_s\, L_{kj}} \delta_{kj} \left(\pi - \left|\delta_{kj}\right|\right); \quad k = 1, 2, 3. \tag{12}$$

$$I_k = \frac{P_k}{V_k} = \sum_{j \neq k}^{3} \frac{V'_j}{2\,\pi^2\, f_s\, L_{kj}} \delta_{kj} \left(\pi - \left| \delta_{kj} \right| \right); \quad k = 1, 2, 3. \tag{13}$$

The relationships (13) highlight that the current I_k is related to the phase displacement (14) through a non-linear function $f(\delta_{kj})$. However, linearization can be performed by (15), limiting δ_{kj} in a range between $\mp\, \pi/5$:

$$f(\delta_{kj}) = \delta_{kj} \left(\pi - \left| \delta_{kj} \right| \right); \tag{14}$$

$$f(\delta_{kj}) \cong \frac{8}{\pi}\, \delta_{kj} \quad for \; -\frac{\pi}{5} \leqslant \delta_{kj} \leqslant \frac{\pi}{5}; \tag{15}$$

Under these assumptions, the TAB model assumes the linear form reported in (16) where the terms $a_{rc} \neq 0$ (with $r, c = 1, 2, 3$), reported in (17), are constant. The linearised TAB model clearly shows the presence of current cross-coupling phenomena.

However, if the leakage inductance of one TAB's port equals zero, the cross-coupling disappears, and the TAB model assumes a decoupled form. For instance, if port no. 1 is set as master, the inductances L_{jk} assume the values $L_{12} = L'_2$, $L_{23} = \infty$ and $L_{31} = L'_3$, respectively. As a consequence, the terms a_{22} and a_{32} became null and the other ones are strictly related ($a_{11} = -a_{21}$ $a_{13} = -a_{33}$). Therefore, the currents I_2 and I_3 depend only on the phase displacement of their respective voltages concerning that provided by the master port no. 1. The current I_1 provided by the master port is the sum of the other two. Furthermore, due to the infinite value assumed by L_{23}, the zero power circulation condition is always satisfied:

$$\overline{I} = \begin{bmatrix} I_1 \\ I_2 \\ I_3 \end{bmatrix} = \begin{bmatrix} a_{11} & 0 & a_{13} \\ a_{21} & a_{22} & 0 \\ 0 & a_{32} & a_{33} \end{bmatrix} \begin{bmatrix} \delta_{12} \\ \delta_{23} \\ \delta_{31} \end{bmatrix} \tag{16}$$

$$\begin{cases} a_{11} = \dfrac{4\, V'_2}{\pi^3\, f_s\, L_{12}} & a_{13} = -\dfrac{4\, V'_3}{\pi^3\, f_s\, L_{13}} \\ a_{21} = -\dfrac{4\, V_1}{\pi^3\, f_s\, L_{12}} & a_{22} = \dfrac{4\, V'_3}{\pi^3\, f_s\, L_{23}} \\ a_{32} = -\dfrac{4\, V'_2}{\pi^3\, f_s\, L_{23}} & a_{33} = \dfrac{4\, V_1}{\pi^3\, f_s\, L_{13}} \end{cases} \tag{17}$$

This distinctive aspect clearly highlights how the choice of inductances and port configuration directly affects the cross-coupling and the behaviour of the TAB converter and serves as the starting point for achieving a decoupled configuration.

2.3. Effect of Transformer Leakage Inductance

The assumption that leakage inductance is equal to zero is purely theoretical due to the intrinsic presence of leakage flux in MFT and its relative magnitude depends on the transformer design. Therefore, analyzing its effects on inherent hardware decoupling is essential.

Assuming port no. 1 as the master and fixing the same rated output power on ports no. 2 and no. 3, the inductances L'_2 and L'_3 can be designed equal according to (7) and named L. Therefore, the TAB model can be treated by considering the magnitude of the MFT leakage inductance of port no. 1 as a function of L through the parameter α. Hence, the relationships between the TAB leakages inductances assume the form reported in (18). Since the TAB currents I_k are related by (19), the linearised TAB model (16) can be rearranged to express the currents on ports no. 2 and no. 3 as a function of the corresponding phase displacement δ_{1k}. Under this assumption, the TAB model achieves the formulation reported in (20), where M_{12} and M_{13} are the voltage ratios V'_2/V_1 and V'_3/V_1, representing the respective step-up or step-down operative condition if they are greater or less than one, respectively.

The TAB model can be expressed in matrix form as reported in (21) to analyse the characteristics of this multi-input multi-output (MIMO) system. In particular, the structure

of $[A]$ confirms the presence of cross-coupling phenomena because it is not a diagonal identity matrix. In particular, the matrix $[A]$ emphasises the dependence of the cross-coupling effects by the parameters α and M_{1k}. In order to evaluate the impact of leakage inductance on hardware decoupling, let us assume to keep the voltage ratios M_{1k} constant and equal to M. Under this hypothesis, the matrix $[A]$ assumes the form reported in (22). The lower D is compared to one, the smaller the coupling effect will be. Indeed, the matrix $[A]$ assumes a diagonal form, typical of a complete decoupled MIMO when D is equal to zero. Therefore, D represents a normalised parameter that allows for the evaluation of the impact of the control strategy and MFT leakage inductance on the inherent decoupling configuration.

The analysis of the evolution of D vs. α, parameterized with respect to M, as shown in Figure 3, highlights that the coupling effects associated with M variations are negligible for an α value less than 0.05, producing a D variation that is less than 0.05. This result is particularly relevant in applications where master voltage variation occurs, as in the proposed case study.

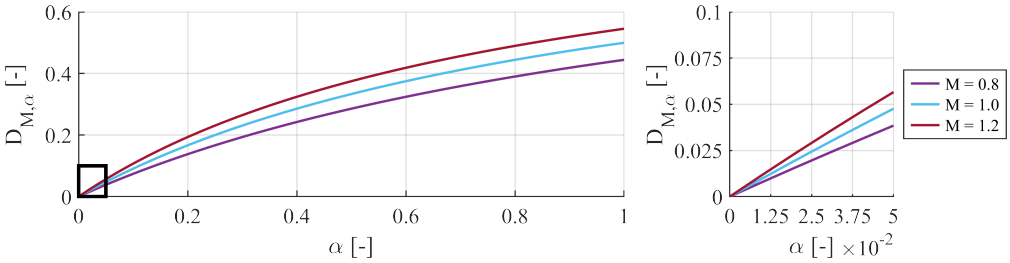

Figure 3. The evolution of the normalized cross-coupling term D vs. α, parametrised for M varying between 1.2 and 0.8.

$$L_2' = L_3' = L; \qquad L_1 = \alpha\, L;$$
$$L_{12} = L_{31} = (2\,\alpha + 1)L; \quad L_{23} = \left(\frac{2\alpha+1}{\alpha}\right)L; \tag{18}$$

$$I_1 + I_2' + I_3' = 0 \tag{19}$$

$$\begin{bmatrix} I_2 \\ I_3 \end{bmatrix} = \frac{4\,V_1}{\pi^3\, f_s\, L}\,\frac{1 + M_{13}\alpha}{2\alpha + 1}\begin{bmatrix} -1 & \dfrac{M_{13}\,\alpha}{1 + M_{13}\,\alpha} \\ \dfrac{M_{12}\,\alpha}{1 + M_{13}\,\alpha} & \dfrac{1 + M_{12}\,\alpha}{1 + M_{13}\,\alpha} \end{bmatrix}\begin{bmatrix} \delta_{12} \\ \delta_{31} \end{bmatrix}; \tag{20}$$

$$\bar{I} = \frac{4\,V_1}{\pi^3\, f_s\, L}\,\frac{1 + M_{13}\alpha}{2\alpha + 1}\;[A]\;\bar{\delta} \tag{21}$$

$$[A] = \begin{bmatrix} -1 & D(M,\alpha) \\ D(M,\alpha) & 1 \end{bmatrix}; \quad D(M,\alpha) = \frac{M\,\alpha}{1 + M\,\alpha}. \tag{22}$$

2.4. TAB Design Methodology for an AEA Application

The definition of an inherently decoupled TAB configuration, aimed at supplying two DC buses of an AEA powered by a single battery pack, requires a specific design methodology. The rated power of the output ports P_2^R and P_3^R and the battery technical specifications are the starting points for the proper hardware and control design of TAB. In particular, the input data are the maximum values of continuous discharge current I_1^{max} and voltage variation ΔV_1 of the battery, together with the rated input and output voltages and powers. The rated output voltages are defined by aeronautic standards at 270 V_{dc} and 28 V_{dc} [3]. The rated power P_2^R and P_3^R depend on the characteristics of the AEA in terms of dimension, flight mission and passengers. Regarding the propulsion system, the

rated power is assumed to be equal to the peak power occurring during take-off. The rated power of the auxiliary system is assumed to be equal to the sum of the rated powers of all the auxiliary equipment with a contemporaneity factor equal to one. The battery cell specifications, jointly with battery pack topology, allow the definition of maximum ΔV_1 for the evaluated power demand in the steady state and during peak power request. This information permits the definition of the main characteristics of MFT in terms of rated power and input/output voltage ratios [22].

The definition of inner leakage inductance of MFT is the consequence of α and L evaluation. The parameter α is chosen initially equal to 0.05 in order to assure the decoupling condition. M is fixed initially equal to one referring to the battery-rated voltage V_{bat} for assuring the maximum TAB zero voltage switching condition extension. Hence, the inductance L can be evaluated for a defined switching frequency f_s as reported in (24) as a function of the rated power and battery voltage. The parameter δ_{12}^{max} is the maximum phase shift value between ports one and two. The δ_{1k}^{max} in DAB design is generally fixed lower than $\pi/2$ for optimising the current stress and efficiency [23]. In the proposed approach, the δ_{12}^{max} is set at $\pi/5$ following the linearization methodology. The proposed modelling allows the design of TAB controllers using linear theory. Considering the avionic standard constraints regarding the bus voltage variations, the DC bus voltages on the auxiliary and propulsion systems must be controlled to keep them constant. For this purpose, the parameter of the PI regulator can be synthesised for each output port referring to the block diagram reported in Figure 4 to achieve the desired bandwidth and rejection to load current disturbance, as follows:

$$I_2^R = \frac{P_2^R}{V_2'} = \frac{4\,V_1}{\pi^3\,f_s\,L}\,\frac{1+\alpha}{2\alpha+1}\,\delta_{12}^{max} \tag{23}$$

$$L = \frac{1+\alpha}{2\alpha+1}\,\frac{4\,V_{bat}^2}{\pi^3\,f_s\,P_2^R}\delta_{12}^{max} \tag{24}$$

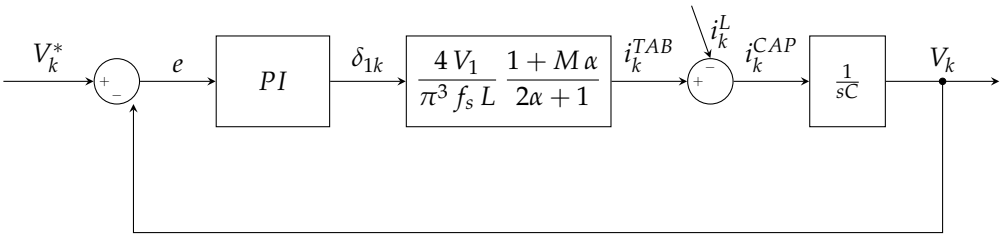

Figure 4. Block diagram of linearised model of inherent decoupled TAB refereed to port no. k with k = 2, 3.

3. Proposed Configuration of TAB

The proposed research activity is aimed to evaluate the TAB performance when it is used for interfacing the two DC buses at 270 V_{dc} (bipolar ±135 V) for the propeller and 28 V_{dc} for the auxiliary power system with the AEA battery pack. Previously studied and developed by authors in works such as [5]), the battery pack design for a specific AEA application (NASA X-57 Maxwell Mod. II) is discussed. The battery pack is composed of series and parallel connections of the commercially available LiB Kokam SLPB100216216H cells, whose main specifications are reported in Table 1. This cell is particularly suitable for aviation applications because it has a continuous output current of 8 C (e.g., 320 A). This feature is significant when high peak power demand is required, as during the take-off and landing of an AEA. The battery pack design was developed to determine the number of cells connected in cascade to form the battery string and the number of strings connected in parallel to achieve the power and energy design targets. The targets for the battery design are shown in Table 2. In particular, the voltage constraints, which must comply with the aircraft voltage standard, relate to the number of cells connected in series N_s. Taking into

account the standardised DC voltage values used in MEA, a nominal battery DC voltage of 270 V was chosen. Table 3 reports the preliminary battery pack design outcomes [22].

Table 1. Kokam SLPB100216216H cell specifications.

Rated Capacity	40 Ah
Discharge Current Limit (8 C)	320 A
Charge Current Limit (3 C)	120 A
Maximum Voltage	4.2 V
Rated Voltage	3.7 V
Minimum Voltage	3.0 V
Weight	940 g
Volume	0.53 L

Table 2. Designed battery pack targets.

Rated Voltage	270 V
Minimum Power Delivered	157 kW
Minimum Energy Delivered	44.2 kWh
Minimum SoC for Energy Backup	30%

Table 3. Designed battery pack configuration.

Series Cells N_s	73
Parallel Modules N_p	7
Peak Power	605 kW
Maximum Energy	76 kWh
Maximum Energy Backup	41.6%
Pack Minimum Weight	480 kg
Pack Minimum Volume	270 L

The inherent decoupled TAB, which guarantees galvanic isolation between the two power systems and an efficient conversion process, is a practical solution for connecting the designed battery pack to the two power systems. In order to evaluate the performance of the proposed configuration, both simulation and experimental investigations were carried out on a scaled prototype.

4. Experimental Set-Up

A test set-up was developed to verify the feasibility of using a TAB as the power conditioning system of an AEA to supply the 270 V and 28 V DC buses. The TAB prototype was designed with a battery pack of 6 kW, distributing 3 kW to the propeller winding at a rated voltage of 270 V and 3 kW to the auxiliary power system at 28 V. The ratio of the three-winding transformer was set at 1:1:0.5 to avoid excessive peak current at the auxiliary output. An interleaved buck converter was connected in series with TAB auxiliary output to comply with the voltage requirement of 28 V.

The TAB consisted of three active bridges, one MFT, and four inductors. Each active bridge was made up of two half-bridges; the main characteristics are presented in Table 4. The half-bridge implements SiC power MOSFETs C2M0080120D; the main characteristics are presented in Table 5. The input and output DC bus capacitance C_{DC}^{tot} of each active bridge equals 520 µF.

Table 4. Half-bridge module rating.

DC Bus voltage V_{DC}	800 V
Maximum continuous current I^{max}	24 A_{RMS}
Maximum pulsed current I_{DC}^{pulsed}	80 A
reference switching frequency f_s	20 kHz
DC side bus capacitance C_{DC}	260 µF

Table 5. SiC Mosfet C2M0080120D maximum ratings.

Drain-Source Voltage V_{ds}	1200 V
Continuous Drain Current I_D^{SiC}	24 A
Power Dissipation P_D^{SiC}	192 W
reference switching frequency f_{sw}	20 kHz
Drain-Source On-State Resistance R_{ds}^{on}	128 mΩ
Turn-On Switching Energy E_{on}^{sw}	265 µJ
Turn-Off Switching Energy E_{off}^{sw}	135 µJ

The main parameters of the three-winding transformer connecting the three active bridges are in Table 6. Four additional ferrite-based inductors are distributed on both the transformer output sides. In particular, two have a rated inductance of 50 µH and a resistance of 0.1 Ω each and are positioned on the transformer 1:1 output side. The two other inductors, having 12.5 µH and 0.05 Ω each, are installed on the transformer 1:0.5 output side. For the proposed configuration, α is equal to 0.02; therefore, following the discussion in Section 2.3, the resulting D value is equal to 0.019, assuring the achievement of the quasi-decoupling condition. Figure 5 shows the developed TAB test bench. The following describes the developed TAB control strategy used for managing its start-up stage and output voltage control:

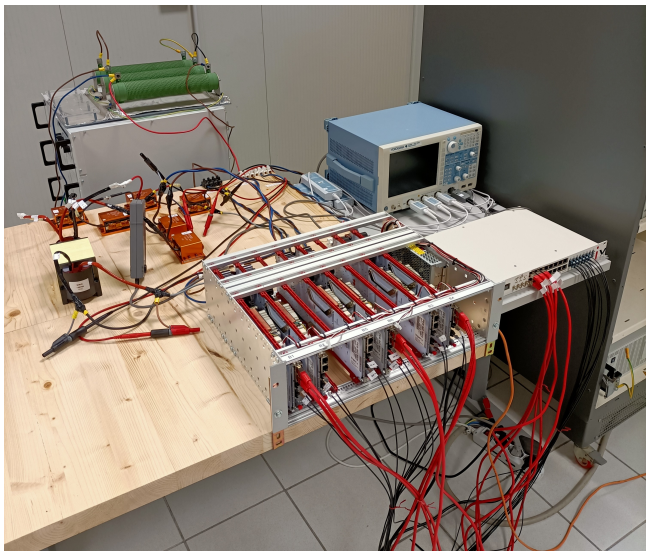

Figure 5. Test bench of TAB.

Table 6. Transformer parameters.

Power Rating P_r	10 + 10 kVA
Transformer voltage ratio n	1:1:0.5
Rated voltage V_1	700 V
Rated switching frequency f_s	20 kHz
Leakage inductance L_1	2 µH
External leakage inductance 1:1 L_2	100 µH
External leakage inductance 1:0.5 L_3	25 µH
Magnetization inductance L_m	1700 µH

Control Strategy

Figure 6 shows a schematic representation of the TAB control strategy. In order to overcome the occurrence of high inrush currents at the beginning of the modulation of the bridges, the start-up phase is necessary. The DC bus capacitors of both output active bridges are not charged. The output bridges act as simple rectifiers, while only the bridge connected to port no. 1 modulates in the start-up phase to limit inrush currents. In addition, to vary the duty cycle and hence the amplitude of the voltage impressed on the MFT, a phase shift τ is imposed between the two primary half-bridge modulation signals. In particular, τ is varied linearly in an open-loop state between 0° and 180° in a time interval of 0.273 s, allowing the transition of the duty cycle of the voltage v_1 from zero to 50%. Thus, the output DC buses are charged with limited currents. The output bridges of terminals no. 2 (propeller side) and no. 3 (auxiliary side) are ready for modulation when τ finishes its evolution.

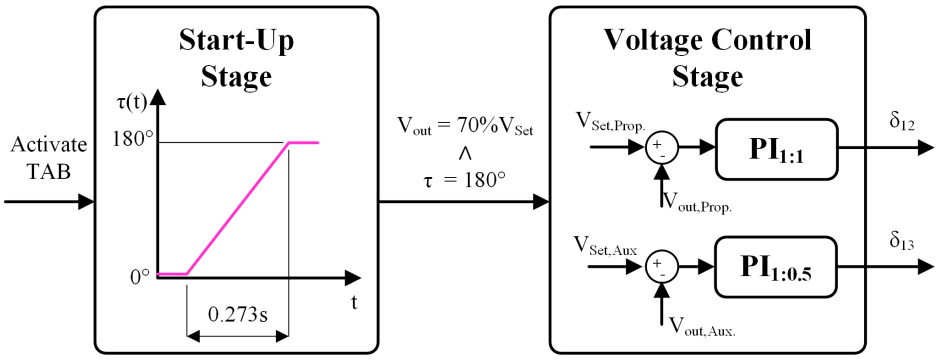

Figure 6. Control strategy of the TAB.

The voltage regulation is activated when τ reaches the steady state value of 50%, thus completing the start-up phase of the charge and maintaining its set points even if a variation in the load occurs. The two output voltages are controlled by two PI controllers according to the model presented in Section 2; the coefficients and time constants are shown in Table 7. In particular, it can be seen that the two time constants are very similar, which means that the two PI controllers have a similar dynamic response when the system is perturbed by a load variation.

Table 7. Parameters of the PI voltage controls.

	Output 1:1	**Output 1:0.5**	
K_p	10^{-3}	7×10^{-4}	/
K_i	2×10^{-4}	13×10^{-2}	/
t	5×10^{-2}	5×10^{-2}	s

The following section reports the simulation study and the experimental results performed on the TAB prototype described in Section 4, particularly concerning the start-up dynamics, voltage control and power coupling phenomenon.

5. Comparison Between Simulation and Experimental Results

The proposed inherent decoupled TAB configuration has been initially analysed by a simulation study performed through a co-simulation integrating Plecs and Matlab/Simulink environments. In particular, the TAB hardware structure has been simulated on Plecs, and the feedback signals are sampled at the frequency f_s and then processed in Matlab/Simulink to provide the modulation signal as output at the Plecs platform, according to the control strategy proposed. The start-up and the voltage control in steady state and during step-load application have been simulated and then experimentally validated on the prototype. In the following, the comparison between simulation and experimental results is reported and discussed.

The simulation and experimental tests during the system start-up stage were performed to analyse the hard-switching conditions and their resulting inrush currents. In particular, during start-up, the DC buses of TAB ports no. 2 and no. 3 are charged from 0 to 270 V and 135 V, imposing an initial load of 243 Ω and 60 Ω, respectively. These load conditions correspond to a steady state power supply of 300 W for each TAB output port. In Figure 7, the simulated and experimental time evolutions of DC output voltages during start-up are shown, highlighting a good matching. In the upper left corner in Figure 7, a focus regarding the time instant in which the closed-loop voltage control is enabled is reported. The results confirmed the start-up procedure's effectiveness because a small voltage compensation is required during the transient associated with voltage control enabling.

The proposed start-up procedure has been initially simulated to avoid the damaging risk of charging inrush currents on active bridges. The simulation results concerning the currents on MFT were then compared with the experimental tests. The results, reported in Figures 8 and 9, show an overlapping between the simulation and experimental underlining that the peak of currents I_2 and I_3 achieves 8 and 10 A, respectively, well below the current limits of power electronic components implemented. Moreover, they confirm the strength of the simulation tool developed.

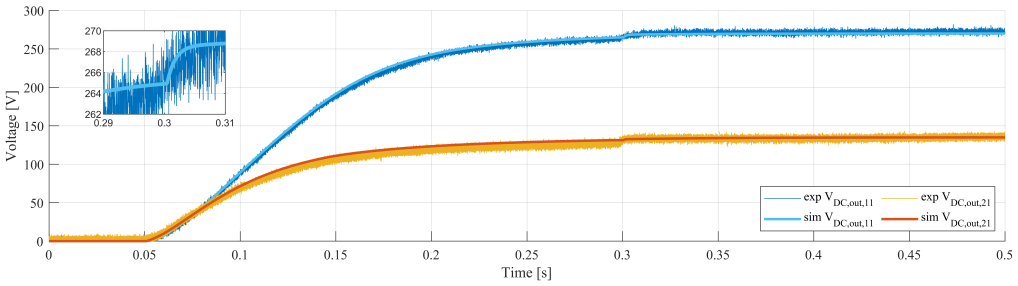

Figure 7. Simulated and experimental output voltages of TAB during start-up.

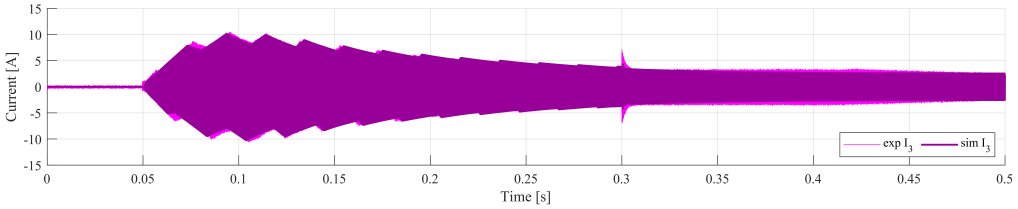

Figure 8. Simulated and experimental auxiliary side currents of TAB during start-up.

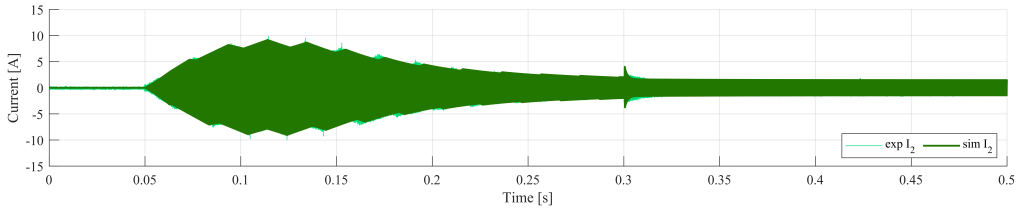

Figure 9. Simulated and experimental propeller side currents of TAB during start-up.

Subsequently, the analysis of TAB performances in steady state has been developed. In Figure 10, the voltage and current time evolution during two periods from both simulations and experimental tests are reported, considering a power demand of 1 kW on both output DC sides. In particular, in Figure 10a,b, the simulated waveforms are shown, while Figure 10c,d report the corresponding measurements of the experimental test. The blue waveforms are related to the transformer input side (port no. 1), the yellow ones show the propeller side (port no. 2), and the red traces show the auxiliary side (port no. 3). The comparison between the simulation and experimental results confirms a good overlap. In order to test the TAB behaviour for higher output power, simulations and experimental tests for a power demand equal to 2 kW on the propeller side and 1 kW on the auxiliary side were executed. Figure 11 presents the voltage and current waveforms from simulations and experimental tests. In particular, in Figure 11a,b the simulated signals are shown, while Figure 11c,d report the experimental ones. The blue waveforms are related to the transformer input side, the yellow ones represent the propeller side, and the red ones represent the auxiliary side.

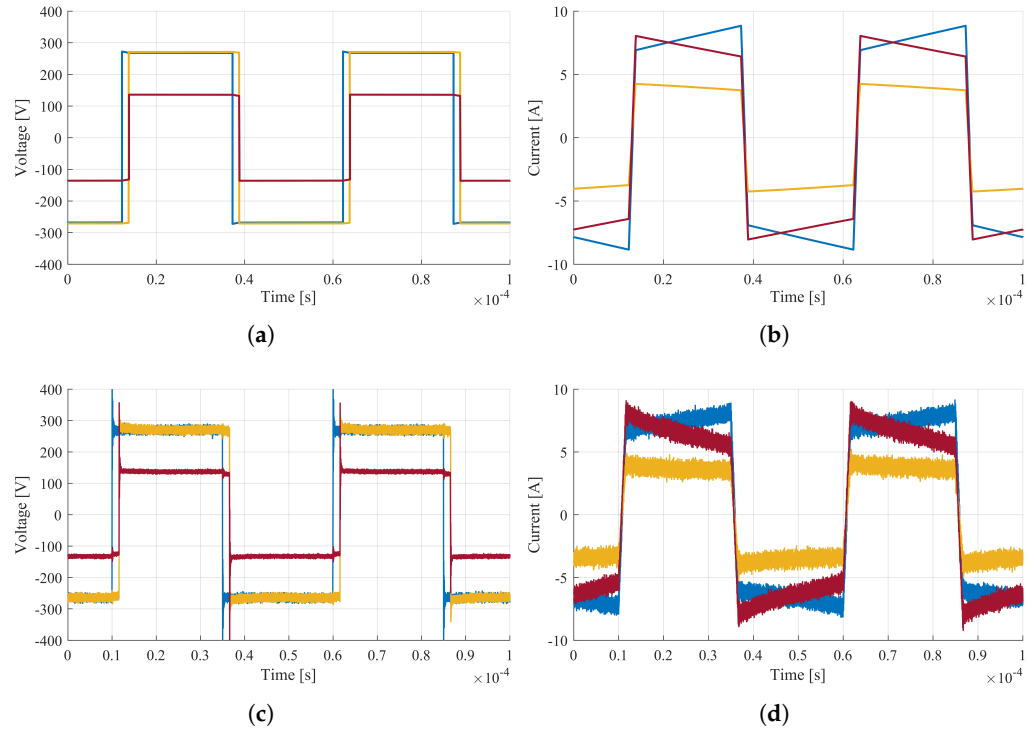

Figure 10. Voltages and currents on the TAB transformer for an output power of 1 kW on each output port: Simulated voltage (**a**) and current (**b**) waveforms; experimental voltage (**c**) and current (**d**) measurement results.

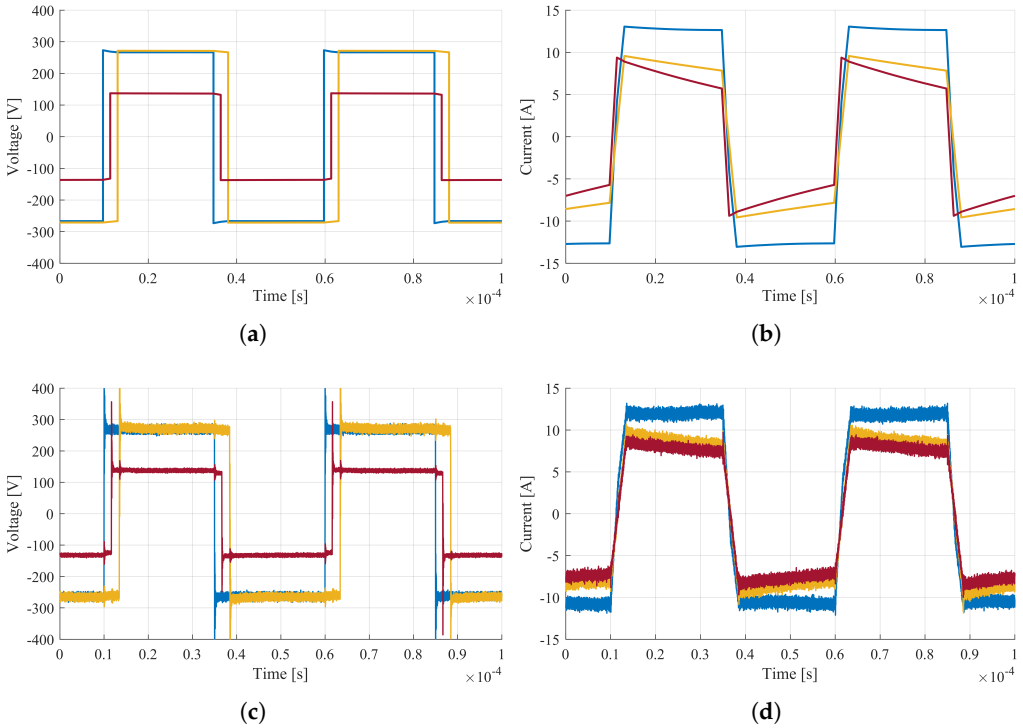

Figure 11. Voltages and currents on TAB transformer for an output power of 2 kW on port no. 2 amd 1 kW on port no. 3: Simulated voltage (**a**) and current (**b**) waveforms; Experimental voltage (**c**) and current (**d**) measurement results.

A simulation study under step-load variations was developed and then experimentally validated to test the effectiveness of inherent power decoupling of the proposed TAB topology. Specifically, the tests were performed by imposing a step-load variation on one port, keeping the power demand constant on the other one. The time evolution of the current and voltage on the port at constant power demand during step load variation gives direct evidence of coupling phenomena. In particular, the magnitude of perturbation concerning the constant set-point during the step variation on the other ports quantifies the coupling effect. The first test was developed by imposing a constant load equal to 72 Ω on the propeller side (port no. 2), corresponding to a load power equal to 1 kW. A step-load variation from 36.5 Ω to 20 Ω (from 500 W to 1 kW) at 0.25 s on the DC auxiliary output port is then applied. In Figure 12, the simulated and experimental time evolution of DC voltages and currents on ports no. 2 and no. 3 are shown. The results confirm the excellent matching between simulated and experimental waveforms and the absence of coupling effects because the DC voltage and current on port no. 2 are unaffected by significant perturbation during step load application. The same outcome is achieved by performing the complementary test for a higher step load variation. In particular, a load step variation from 146 Ω to 36.4 Ω has been carried out, allowing for the propeller side a variation in power consumption from 500 W to 2 kW. The auxiliary side load has been kept constant, equalling 20 Ω (1 kW). In Figure 13, the DC voltages and currents on ports no. 2 and no. 3 are reported, confirming the effectiveness of the proposed approach.

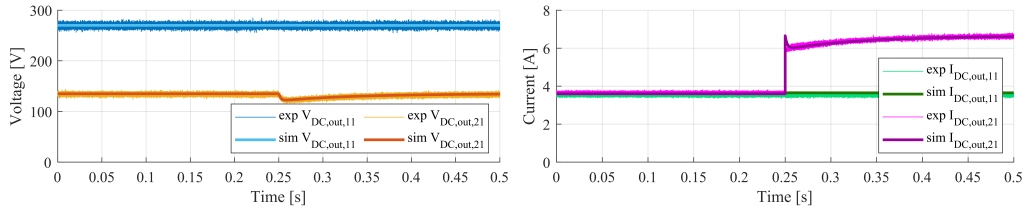

(**a**) (**b**)

Figure 12. Comparison of simulated and experimental output voltages (**a**) and currents (**b**) of TAB during load variation on the auxiliary side from 36.5 Ω to 20 Ω.

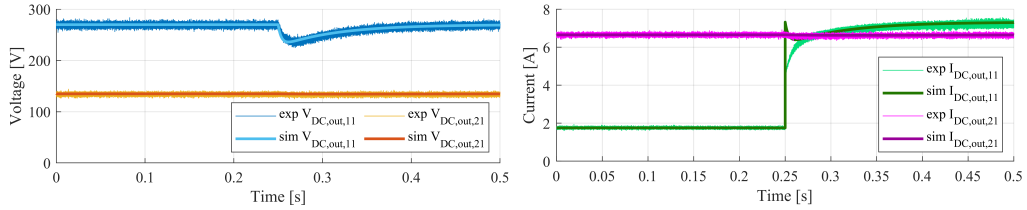

(**a**) (**b**)

Figure 13. Comparison of simulated and experimental output voltages (**a**) and currents (**b**) of TAB during load variation on the propeller side from 146 Ω to 36.4 Ω.

The phase-shift values of the simulation study are not reported here since their deviation from the experimental one is less than 2%, presenting a good superimposition. From both simulation and experimental tests, it can be observed that a load variation on the propeller side output does not result in appreciable perturbations on the auxiliary side output voltage (let alone the current). The same can be said during the load variation on the auxiliary side, being able to assume that the mutual dependence between the transformer outputs is negligible. This behaviour clearly demonstrates how the removal of the external inductor on the port acting as the "master" side, combined with a proper design of the MFT and external leakage inductors, enables the possibility of treating the TAB as decoupled DC/DC power conditioning systems in the considered power range. Although it is not the primary focus of this study, it is worth noting that the system efficiency reaches a value equal to 92%. Furthermore, it is important to clarify that both the transformer and the converters were oversized relative to the power levels used during the tests. As a result, despite the system being tested at a low load (approximately 20% of their nominal power), the TAB converter managed a power flow of about 3 kW with a conversion efficiency, which can still be considered high, assessing the performances of this DC power system employed for an application such as interfacing an AEA battery power supply.

6. Conclusions

This paper evaluates a power conditioning system for interconnecting the battery pack to the DC power systems in an ultra-light all-electric aircraft. The focus is on a triple-active bridge in its inherent decoupled configuration. The linear formulation TAB model has been investigated to define the effects of decoupling in reducing the leakage inductance of one port concerning the others. Furthermore, the voltage ratios between the master and output ports have been considered. The proposed linear model supported the hardware and software TAB design of a scaled configuration of an ultra-light all-electric aircraft power system. The model of the proposed power conditioning prototype was first simulated and then experimentally validated. The results demonstrate a good correlation between the simulation and experimental tests. The experimental validation confirms the expected performance during start-up and step load application. Additionally, implementing a snubber-less TAB configuration and the specific power control range has enabled the quasi-decoupled power flow and voltage management. Thus, the proposed

inherent decoupled TAB configuration is suitable for interfacing the AEA's battery pack with its DC power systems. Moreover, the proposed inherent decoupled triple-active bridge (TAB) configuration demonstrates significant potential compared to conventional systems, such as configurations involving one battery and one converter for the propeller and a separate battery and converter for auxiliary systems. The decoupled TAB provides a unified solution that reduces component redundancy and enhances power flow flexibility, making it particularly advantageous for ultra-light all-electric aircraft (AEA). Future developments will focus on optimising the design to further enhance the system applicability to AEA. This includes detailed weight analysis and transitioning from prototype-level designs to converters and transformers specifically optimised for lightweight applications. By addressing these challenges, the proposed system could contribute to advancing AEA technologies, paving the way for more efficient and compact power systems tailored to meet the rigorous demands of next-generation electric aviation.

Author Contributions: Conceptualization, G.B. and A.D.; methodology, A.D.; software, G.B. and N.C.; validation, G.B., N.C. and M.B.; formal analysis, A.D.; investigation, G.B. and N.C.; resources, A.D.; data curation, G.B. and N.C.; writing—original draft preparation, A.D. and N.C.; writing—review and editing, G.B., N.C., M.B., R.M., and A.D.; visualization, N.C.; supervision, R.M. and A.D.; project administration, R.M. and A.D.; funding acquisition, R.M. and A.D. All authors have read and agreed to the published version of the manuscript.

Funding: This work was partially funded by the National Recovery and Resilience Plan (NRRP), Mission 4 Component 2 Investment 1.3—Call for tender No. 1561 of 11.10.2022 of Ministero dell'Università e della Ricerca (MUR); funded by the European Union—NextGenerationEU. Award Number: Project Code code PE0000021, Concession Decree No. 1561 of 11.10.2022 adopted by Ministero dell'Università e della Ricerca (MUR), CUP F53C22000770007, Project title "Network 4 Energy Sustainable Transition—NEST" and by the project 'SiciliAn MicronanOTecH Research And Innovation CEnter' 'SAMOTHRACE' (MUR, PNRR-M4C2, ECS-00000022), spoke 3—Universita degli "Studi di Palermo 'S2-COMMs'—Micro and Nanotechnologies for Smart and Sustainable Communities".

Data Availability Statement: The original contributions presented in the study are included in the article, further inquiries can be directed to the corresponding author.

Acknowledgments: This work was developed within the project funded under the National Recovery and Resilience Plan (NRRP), Mission 4 Component 2 Investment 1.3—Call for tender No. 1561 of 11.10.2022 of Ministero dell'Università e della Ricerca (MUR); funded by the European Union—NextGenerationEU. Award Number: Project Code code PE0000021, Concession Decree No. 1561 of 11.10.2022 adopted by Ministero dell'Università e della Ricerca (MUR), CUP F53C22000770007, Project title "Network 4 Energy Sustainable Transition—NEST" and by the project 'SiciliAn MicronanOTecH Research And Innovation CEnter' 'SAMOTHRACE' (MUR, PNRR-M4C2, ECS-00000022), spoke 3—Universita degli "Studi di Palermo 'S2-COMMs'—Micro and Nanotechnologies for Smart and Sustainable Communities".

Conflicts of Interest: The authors declare no conflicts of interest.

References

1. Howse, M. All electric aircraft. *Power Eng.* **2003**, *17*, 35–37. [CrossRef]
2. Wheeler, P. Technology for the more and all electric aircraft of the future. In Proceedings of the 2016 IEEE International Conference on Automatica (ICA-ACCA), Curico, Chile, 19–21 October 2016; pp. 1–5. [CrossRef]
3. Barzkar, A.; Ghassemi, M. Electric Power Systems in More and All Electric Aircraft: A Review. *IEEE Access* **2020**, *8*, 169314–169332. [CrossRef]
4. Turpin, C.; Morin, B.; Bru, E.; Rallieres, O.; Roboam, X.; Sareni, B.; Garcia Arregui, M.; Roux, N. Power for Aircraft Emergencies: A Hybrid Proton-Exchange Membrane H_2O_2 Fuel Cell and Ultracapacitor System. *IEEE Electrif. Mag.* **2017**, *5*, 72–85. [CrossRef]
5. Campagna, N.; Castiglia, V.; Damiano, A.; Di Noia, L.P.; Miceli, R.; Di Tommaso, A.O. A Hybrid Energy Storage Sizing for a Vertical Take-off and Landing Electric Aircraft. In Proceedings of the IECON 2021—47th Annual Conference of the IEEE Industrial Electronics Society, Toronto, ON, Canada, 13–16 October 2021; pp. 1–6. [CrossRef]
6. Raymond, A.R.; Speth, L.; Sabnis, J.S.; Barrett, S. Technical and environmental assessment of all-electric 180-passenger commercial aircraft. *Prog. Aerosp. Sci.* **2019**, *105*, 1–30.

7. Damiano, A.; Porru, M.; Salimbeni, A.; Serpi, A.; Castiglia, V.; Di Tommaso, A.O.; Miceli, R.; Schettino, G. Batteries for Aerospace: A Brief Review. In Proceedings of the 2018 AEIT International Annual Conference, Bari, Italy, 3–5 October 2018; pp. 1–6. [CrossRef]
8. Cao, W.; Zhang, J.; Li, H. Batteries with high theoretical energy densities. *Energy Storage Mater.* **2020**, *26*, 46–55. [CrossRef]
9. Boscaino, V.; Miceli, R.; Capponi, G. MATLAB-based simulator of a 5 kW fuel cell for power electronics design. *Int. J. Hydrogen Energy* **2013**, *38*, 7924–7934. [CrossRef]
10. Swaminathan, N.; Cao, Y. An Overview of High-Conversion High-Voltage DC–DC Converters for Electrified Aviation Power Distribution System. *IEEE Trans. Transp. Electrif.* **2020**, *6*, 1740–1754. [CrossRef]
11. Buticchi, G.; Costa, L.F.; Barater, D.; Liserre, M.; Amarillo, E.D. A Quadruple Active Bridge Converter for the Storage Integration on the More Electric Aircraft. *IEEE Trans. Power Electron.* **2018**, *33*, 8174–8186. [CrossRef]
12. Keilmann, R.; Radomsky, L.; Ferch, D.; Mallwitz, R. Study of Inverter Topologies for Electrified Aircraft Propulsion Systems Based on Cyclic Loading Induced Bond Wire Fatigue. In Proceedings of the 2024 Energy Conversion Congress and Expo Europe (ECCE Europe), Darmstadt, Germany, 2–6 September 2024; pp. 1–8. [CrossRef]
13. Ge, L.; Du, N.; Song, J.; Zhang, J.; Fan, Z.; Zhang, D.; Song, S. Advanced Technology of Switched Reluctance Machines in More Electric Aircraft: A Review. *IEEE Trans. Power Electron.* **2025**, *40*, 195–216. [CrossRef]
14. Wang, X.; Atkin, J.; Yeoh, S.S.; Bozhko, S. Choice of Optimal Voltage for DC Power Distribution Systems on More Electric Aircraft. In Proceedings of the 2024 Energy Conversion Congress and Expo Europe (ECCE Europe), Darmstadt, Germany, 2–6 September 2024; pp. 1–6. [CrossRef]
15. Sarlioglu, B.; Morris, C.T. More Electric Aircraft: Review, Challenges, and Opportunities for Commercial Transport Aircraft. *IEEE Trans. Transp. Electrif.* **2015**, *1*, 54–64. [CrossRef]
16. Wang, L.; Wang, Z.; Li, H. Asymmetrical Duty Cycle Control and Decoupled Power Flow Design of a Three-port Bidirectional DC-DC Converter for Fuel Cell Vehicle Application. *IEEE Trans. Power Electron.* **2012**, *27*, 891–904. [CrossRef]
17. Bandyopadhyay, S.; Purgat, P.; Qin, Z.; Bauer, P. A Multiactive Bridge Converter With Inherently Decoupled Power Flows. *IEEE Trans. Power Electron.* **2021**, *36*, 2231–2245. [CrossRef]
18. Chen, Y.M.; Liu, Y.C.; Wu, F.Y. Multi-input DC/DC converter based on the multiwinding transformer for renewable energy applications. *IEEE Trans. Ind. Appl.* **2002**, *38*, 1096–1104. [CrossRef]
19. Zhao, C.; Round, S.D.; Kolar, J.W. An Isolated Three-Port Bidirectional DC-DC Converter with Decoupled Power Flow Management. *IEEE Trans. Power Electron.* **2008**, *23*, 2443–2453. [CrossRef]
20. Tao, H.; Duarte, J.L.; Hendrix, M.A.M. Three-Port Triple-Half-Bridge Bidirectional Converter with Zero-Voltage Switching. *IEEE Trans. Power Electron.* **2008**, *23*, 782–792. [CrossRef]
21. Zhao, C.; Kolar, J. A novel three-phase three-port UPS employing a single high-frequency isolation transformer. In Proceedings of the 2004 IEEE 35th Annual Power Electronics Specialists Conference (IEEE Cat. No.04CH37551), Aachen, Germany, 20–25 June 2004; Volume 6, pp. 4135–4141. [CrossRef]
22. Bossi, G.; Floris, A.; Campagna, N.; Miceli, R.; Damiano, A. Design of a Battery Pack for the Power System of an All-Electric Aircraft by Cell Characterization. In Proceedings of the 2023 International Conference on Clean Electrical Power (ICCEP), Terrasini, Italy, 27–29 June 2023; pp. 76–82. [CrossRef]
23. Rodríguez, A.; Vázquez, A.; Lamar, D.; Hernando, M.M.; Sebastián, J. Different Purpose Design Strategies and Techniquesto Improve the Performance of a Dual Active Bridge with Phase-Shift Control. *IIEEE Trans. Power Electron.* **2015**, *30*, 790–804. [CrossRef]